

Large-Eddy Simulations of Convective Boundary Layers over Flat and Urbanlike Surfaces

SEUNG-BU PARK AND JONG-JIN BAIK

School of Earth and Environmental Sciences, Seoul National University, Seoul, South Korea

(Manuscript received 28 June 2013, in final form 13 January 2014)

ABSTRACT

The effects of urbanlike surfaces with a block array on the dry convective boundary layer (CBL) are numerically investigated using the parallelized large-eddy simulation model. Five cases representing a free CBL, a sheared CBL, and a strongly sheared CBL over flat surfaces, a sheared CBL over a block array, and a sheared CBL over a modeled canopy layer are simulated and compared. In the sheared CBL over a block array, mixed-layer flow is decelerated because of increased surface shear and horizontal convective rolls appear in the mixed layer. In contrast, convection cells and intermediate structures between cells and rolls occur in the free and sheared CBLs over flat surfaces, respectively. Horizontal convective rolls and the traces of block-induced turbulent eddies are detected in the spectral density fields of vertical velocity and in the vertical profiles of vertical velocity skewness in the sheared CBL over a block array. The decelerated mixed-layer flow in the sheared CBL over a block array leads to stronger wind shear in the entrainment zone than in the other cases, resulting in streamwise alternating updrafts and downdrafts there. While the contributions to vertical turbulent heat flux by rising cool air and sinking cool air are dominant in the free CBL, the contributions to vertical turbulent heat flux by sinking warm air and rising warm air increase as the wind shear in the entrainment zone increases. Because of enhanced turbulence activity and wavelike motions in the entrainment zone, the magnitude of entrainment heat flux in the CBL over a block array is larger than that in the other cases.

1. Introduction

It is well known that buildings in urban areas can affect street- to city-scale flow and pollutant dispersion. Furthermore, urban areas, which are composed of buildings and streets, can induce horizontal convergence and secondary circulation by large surface roughness (Kropfli and Kohn 1978; Miao and Chen 2008). Using a dual-Doppler radar system, Kropfli and Kohn (1978) observed persistent horizontal convective rolls (HCRs) in the convective boundary layer over a large urban area. Miao and Chen (2008) also observed cloud streets (a manifestation of HCRs) in the satellite imagery and showed through numerical simulations that HCRs usually occur in urban areas when the atmospheric stability satisfies a certain criterion ($-z_i/L < 25$, where z_i is the

inversion height and L is the Monin–Obukhov length) while convection cells frequently occur in rural areas.

Many studies have focused on the structure of the convective boundary layer (CBL) over a flat surface or entrainment process at the CBL top (LeMone 1973; Moeng and Sullivan 1994; Khanna and Brasseur 1998; Kim and Park 2003; Kim et al. 2003; Conzemius and Fedorovich 2006; Miao et al. 2006). Moeng and Sullivan (1994) simulated several CBLs using a large-eddy simulation (LES) model and compared the free (without background wind) CBL and sheared CBL flows. Based on LES data, they highlighted the importance of surface shear in the entrainment process and proposed a new velocity scale—a combination of convective velocity and surface friction velocity—to approximate the entrainment heat flux. Kim et al. (2003) investigated the effects of wind shear on the entrainment process. They found that shear instability induces wavelike motions at the top of HCRs. Conzemius and Fedorovich (2006) also emphasized the importance of wind shear, especially in the entrainment zone, in enhancing CBL entrainment. They reported that surface shear indirectly affects wind shear

Corresponding author address: Jong-Jin Baik, School of Earth and Environmental Sciences, Seoul National University, Seoul 151-742, South Korea.
E-mail: jjbaik@snu.ac.kr

in the entrainment zone by decelerating the flow of the CBL interior. Pino and Vilà-Guerau de Arellano (2008) reported that the CBL deepens with increasing geostrophic wind speed and the velocity jump and momentum fluxes at the inversion height are important to entrainment processes. These studies of CBLs over flat surfaces are very valuable. As an extension of previous studies, it would be of interest to examine CBLs over urban areas that are characterized by large surface roughness.

Lin et al. (1997) investigated the effects of surface roughness on flow in a planetary boundary layer using an LES model. They showed that as the surface roughness increases, ejection eddies and vortical structures increase in scale as well as in strength. Emeis et al. (2007) and Barlow et al. (2008) showed that the profiles of wind and turbulence in urban boundary layers are sensitive to upwind surface roughness by analyzing sodar measurements. Using a dual-Doppler radar system, Iwai et al. (2008) showed that uprising parts of HCRs (in the sea-breeze internal boundary layer) originate in near-surface flow structures such as low-speed streaks. Low-speed streaks are known to be characteristic flow structures in urban surface layers (Coccal et al. 2007; Newsom et al. 2008; Inagaki and Kanda 2010). Thus, turbulent eddies induced by roughness elements in urban areas are expected to affect the formation of CBL flow structures and also entrainment process at the CBL top.

Although the surface roughness is important to turbulence structures and the entrainment process in the CBL, previous studies have been focused mainly on the neutral or convective boundary layer over flat surfaces. Thus, further studies that investigate the effects of roughness elements on the CBL are necessary. Castillo et al. (2011) and Inagaki et al. (2012) simulated CBLs over an urbanlike surface by explicitly resolving flow around a cubical building array, focusing on the inertial-sublayer turbulence. Kanda et al. (2013) simulated boundary layers over realistic urban morphologies, focusing on aerodynamic parameters of the urban morphologies. There is, to the authors' knowledge, no study that investigates the CBL over an urbanlike surface and entrainment process.

In this study, we examine the turbulence structures of a dry CBL over an urbanlike surface with a block array and the effects of the block array on the entrainment process using an LES model. The LES model and simulation setup are described in section 2. Simulation results are presented and discussed in section 3. Finally, a summary and conclusions are given in section 4.

2. Model description and simulation setup

In this study, the parallelized LES model (PALM) developed at the Leibniz University of Hannover

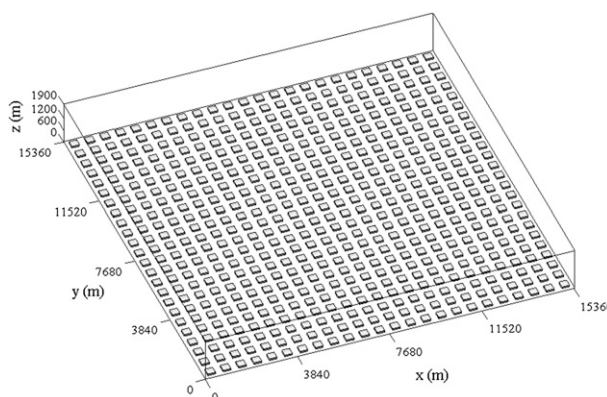


FIG. 1. Illustration of the computational domain and block configuration in the SB case.

(Raasch and Etling 1998; Raasch and Schröter 2001; Letzel et al. 2008) is used to simulate CBLs over flat and urbanlike surfaces. PALM is based on the implicitly filtered Boussinesq equations. The prognostic equations of momentum, thermodynamic energy, and subgrid-scale (SGS) turbulent kinetic energy (TKE) are numerically solved using finite-difference schemes. The third-order Runge–Kutta scheme is used for time integration, and the second-order Piacsek and Williams (1970) scheme is used for advection. The 1.5-order Deardorff (1980) scheme that uses SGS TKE to calculate eddy viscosity is employed to parameterize SGS turbulent fluxes.

To investigate the effects of urbanlike surface with building blocks on turbulence structures of CBL, five cases are simulated: a free CBL over a flat surface (FF), a sheared CBL over a flat surface (SF), a strongly sheared CBL over a flat surface (SSF), a sheared CBL over a block array (SB), and a sheared CBL over a modeled canopy layer (SC). In all cases, PALM is integrated for 2 h and the last 600 s of simulation data are analyzed. In the SC case, the pressure drag is implemented in the canopy layer following the plant-canopy model of Watanabe (2004). The pressure drag ($-c_d a U u_i$) and a sink term of SGS TKE ($-2c_d a U e$) are added in the equations of momentum and SGS TKE, respectively. Here, c_d , a , U , u_i , and e are the drag coefficient, leaf area density, wind speed, i th component of wind velocity, and SGS TKE, respectively. The drag coefficient and leaf area density or their product (the canopy penetration depth; Harman and Finnigan 2007) are required to calculate the pressure drag exerted by blocks. In this study, the relationship of attenuation coefficient and frontal area density for a block array in Macdonald (2000) is used to calculate the canopy penetration depth (instead of c_d and a). By comparing the SB and SC cases, the impacts of physical blocks can be illustrated. Along with the five cases, a free CBL over a block array is also

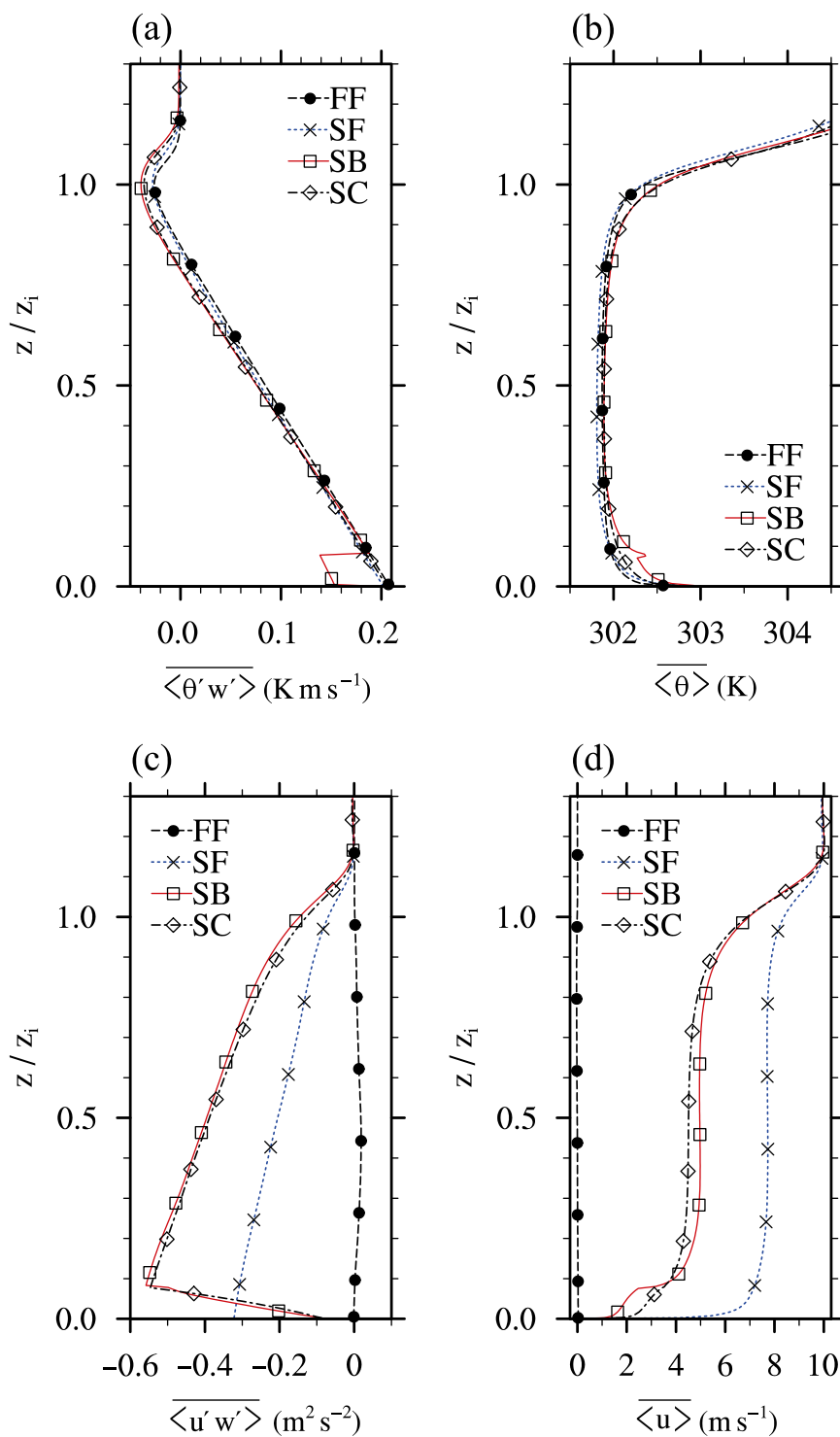


FIG. 2. Vertical profiles of temporally and horizontally averaged (a) vertical turbulent heat flux, (b) potential temperature, (c) vertical turbulent momentum flux, and (d) streamwise velocity in the FF, SF, SB, and SC cases.

TABLE 1. Bottom heat flux (Q_0), geostrophic wind speed (U_g), friction velocity (u_*), convective velocity [$w_* = (gz_i Q_0/T)^{1/3}$, where g is the gravitational acceleration and T is the temperature], the ratio of friction velocity to convective velocity, inversion height (z_i), the ratio of inversion height to the Monin–Obukhov length ($-z_i/L$), the thickness of entrainment zone ($z_{iu} - z_{il}$), difference in streamwise velocity between the upper and lower limits of entrainment zone ($\langle u \rangle_{z_{iu}} - \langle u \rangle_{z_{il}}$), turbulent heat flux at the inversion height ($\langle \theta' w' \rangle_{z_i}$), and the ratio of vertical turbulent heat flux at the inversion height to bottom heat flux ($-\langle \theta' w' \rangle_{z_i}/Q_0$) in the FF, SF, SSF, SB, and SC cases.

	FF	SF	SSF	SB	SC
Q_0 (K m s^{-1})	0.2	0.2	0.2	0.2	0.2
U_g (m s^{-1})	0	10	15	10	10
u_* (m s^{-1})	0.03	0.57	0.74	0.64	0.76
w_* (m s^{-1})	1.87	1.87	1.87	1.88	1.89
u_*/w_*	0.02	0.31	0.40	0.34	0.40
z_i (m)	1005	995	1005	1025	1035
$-z_i/L$	71 416.8	14.1	6.4	10.2	6.2
$z_{iu} - z_{il}$ (m)	250	290	360	400	360
$\langle u \rangle_{z_{iu}} - \langle u \rangle_{z_{il}}$ (m s^{-1})	0.04	2.12	3.76	4.86	5.08
$\langle \theta' w' \rangle_{z_i}$ (K m s^{-1})	-0.026	-0.028	-0.032	-0.039	-0.036
$-\langle \theta' w' \rangle_{z_i}/Q_0$ (%)	13.1	13.9	16.1	19.7	18.2

simulated, but the difference from the FF case is small because of the negligible wind shear in the surface layer.

Figure 1 shows the computational domain and block configuration in the SB case. The computational domain size is 15 360 m in the x (streamwise) direction, 15 360 m in the y (spanwise) direction, and 1900 m in the z (vertical) direction. The grid size in both the x and y directions is 20 m. The grid size in the z direction is uniform with 5 m up to $z = 80$ m and increases with an expansion ratio of 1.08 up to $z \sim 155$ m, then is 10 m above that height. An idealized block array, which is composed of same-sized rectangular blocks (320 m wide, 320 m long, and 80 m high), is considered in the SB case. Because of the limited resolution, an array of large blocks (considering that each block represents a group of buildings) is considered and 16 grids are present in each block length to explicitly resolve flow around each block (Xie and Castro 2006). The blocks are arranged in lines with a constant spacing of 320 m in both the x and y directions. Therefore, the plan area density of the block array is 25% and the aspect ratio of street canyon is 0.25. The cyclic boundary condition is applied at the lateral boundaries for velocity components, temperature, and SGS TKE, and the Dirichlet boundary condition is applied at the top boundary. Westerly geostrophic wind ($U_g = 10 \text{ m s}^{-1}$ in the SF, SB, and SC cases and 15 m s^{-1} in the SSF case) is initially imposed in the model domain, and the Coriolis parameter is evaluated at 37°N . The Coriolis force induces anticlockwise turning of mean wind direction downward in the CBL. The initial potential temperature is constant up to $z = 700$ m and increases upward with a lapse rate of 0.01 K m^{-1} above $z = 700$ m. The magnitude of heat flux at all bottom surfaces (including the tops of blocks in the SB case) is

0.2 K m s^{-1} in all cases. At grid points closest to all the solid surfaces, the Monin–Obukhov (MO) similarity is employed in the momentum equation. The roughness length for momentum is 0.1 m. In the SB case, quantities at the grid points inside the blocks are not prognostically calculated following the mask method in Letzel et al. (2008), and initial values (0 m s^{-1} for velocities and 300 K for potential temperature) inside the blocks are used for averaging procedures. The MO similarity is employed at the sidewalls of the blocks, although the applicability of the MO similarity in unstable stratification is not assured. However, the difference between the SB case and the modified SB case, in which the effect of unstable stratification is artificially neglected, is not significant above the blocks, indicating the small effect of wall boundary conditions on CBLs (not shown). However, further study is required to determine the applicability of the MO similarity at building walls in different stratifications.

3. Results and discussion

a. Turbulence structures

Figure 2 shows the vertical profiles of horizontally averaged (mean) vertical turbulent heat flux ($\langle \theta' w' \rangle$), potential temperature ($\langle \theta \rangle$), vertical turbulent momentum flux ($\langle u' w' \rangle$), and streamwise velocity ($\langle u \rangle$) in the FF, SF, SB, and SC cases. Here, u is the streamwise velocity, w is the vertical velocity, and θ is the potential temperature and u' , w' , and θ' denote deviations from the horizontally averaged variables $\langle u \rangle$, $\langle w \rangle$, and $\langle \theta \rangle$, respectively. In this study, overbars and angle brackets indicate temporal (600 s) and spatial averages. The vertical turbulent heat

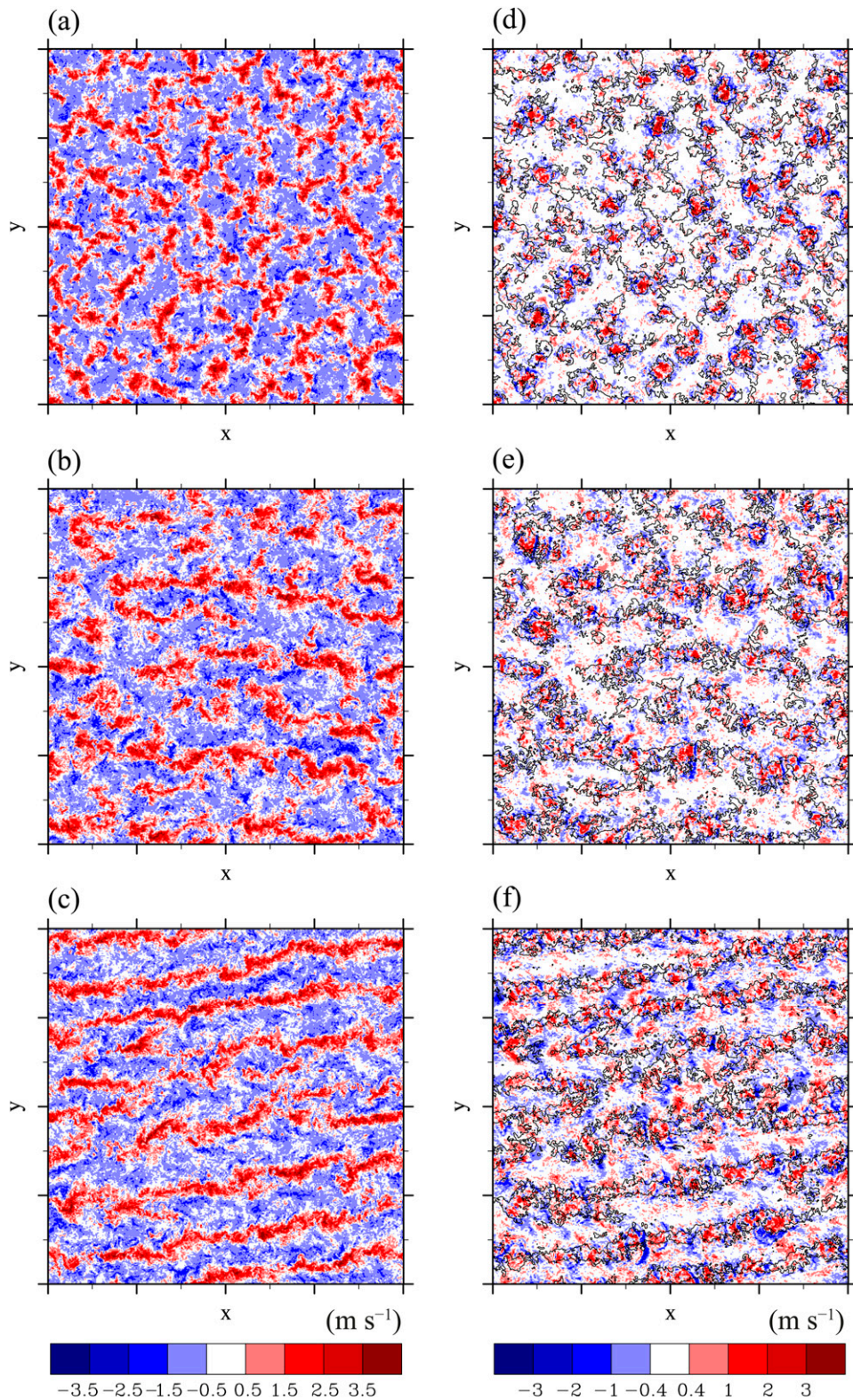


FIG. 3. Vertical velocity fields (left) at $z = 500$ m in the (a) FF, (b) SF, and (c) SB cases and (right) at $z = 1000$ m in the (d) FF, (e) SF, and (f) SB cases at $t = 6900$ s. The contours of vertical velocity (0.5 m s^{-1}) at $z = 500$ m are added in (d)–(f). The x – y plane in this figure is the entire computational domain.

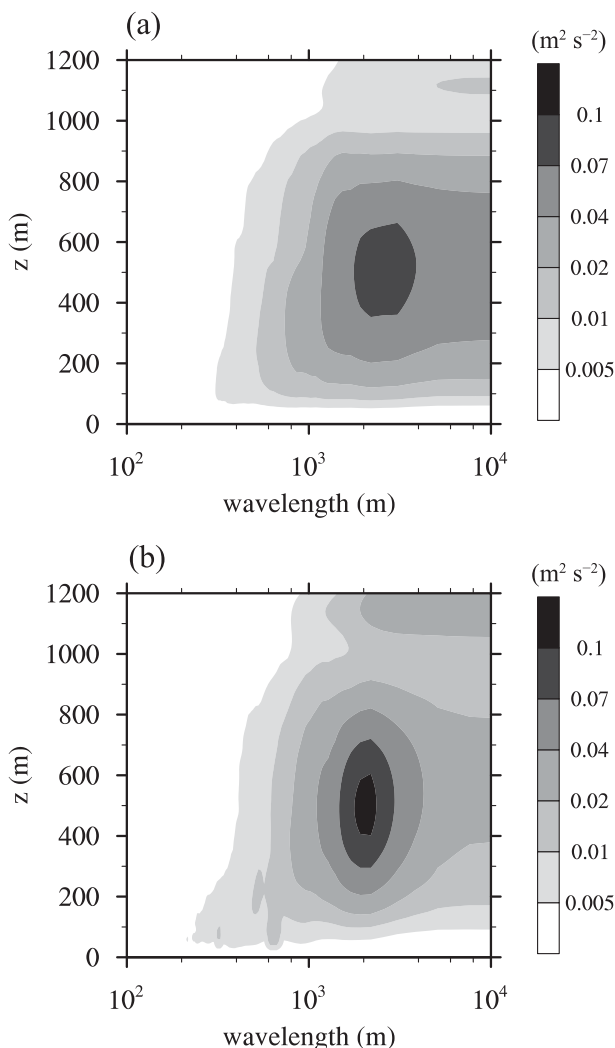


FIG. 4. Spectral density fields of vertical velocity in the λ_y - z plane at $t = 6900$ s in the (a) SF and (b) SB cases.

flux linearly decreases with height from the bottom surface (or block top height in the SB case) to the inversion height in all cases (Fig. 2a). The inversion height here is defined as the height where the vertical turbulent heat flux reaches a minimum value (the entrainment heat flux). The upper limit z_{iu} and lower limit z_{il} of the entrainment zone are determined as the heights where the magnitude of vertical turbulent heat flux are near zero above and below the inversion height, respectively. Calculated quantities, such as surface friction velocity and convective velocity in the five cases, are listed in Table 1. The surface friction velocity is calculated as the square root of the maximum magnitude of (horizontally averaged) vertical turbulent momentum flux in all cases except the SB case. In the SB case, temporally averaged vertical turbulent momentum flux is used to calculate the surface friction velocity because of the existence of

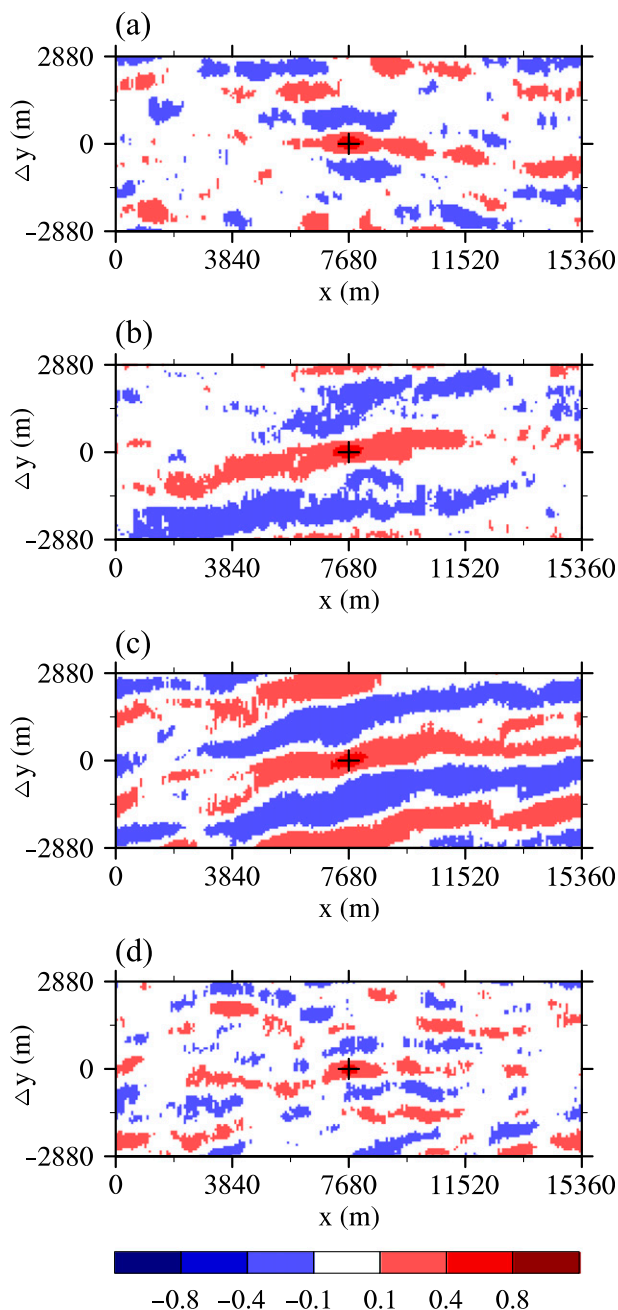


FIG. 5. Temporally averaged fields of space (Δy)-lag cross-correlation coefficient of vertical velocity at $z = 500$ m in the (a) SF, (b) SSF, (c) SB, and (d) SC cases. The reference point is indicated by a cross.

blocks. The magnitude of entrainment heat flux is larger in the SB case ($-0.039 \text{ K m s}^{-1}$) than in the FF and SF cases (-0.026 and $-0.028 \text{ K m s}^{-1}$, respectively). Although the difference in entrainment heat flux magnitude between the FF and SF cases is very small, the thickness of entrainment zone ($z_{iu} - z_{il}$) in the SF case (290 m) is larger than that in the FF case (250 m), indicating more

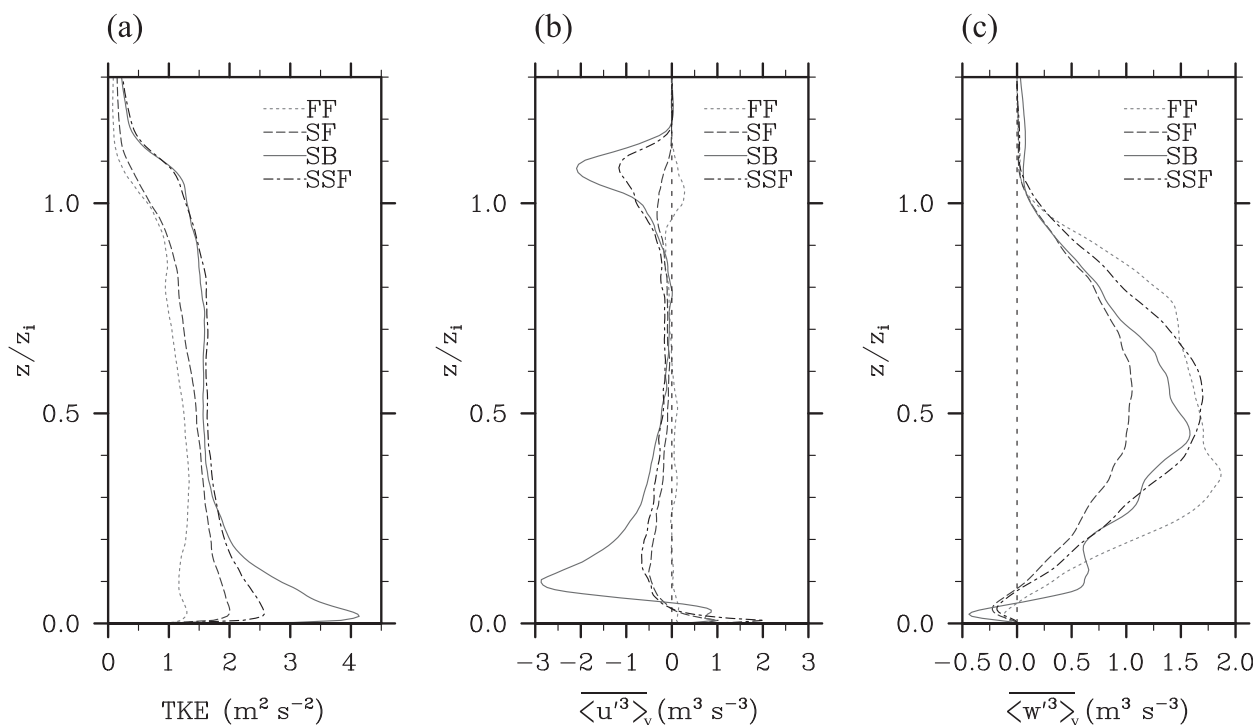


FIG. 6. Vertical profiles of spanwise-averaged (at $x = 7680$ m) (a) turbulent kinetic energy, (b) skewness of streamwise velocity, and (c) skewness of vertical velocity in the FF, SF, SB, and SSF cases.

active entrainment in the SF case. The magnitude of entrainment heat flux in the SC case ($-0.036 \text{ K m s}^{-1}$) is slightly smaller than that in the SB case.

In the mixed layer ($0.1z_i < z < z_{il}$), the potential temperature is nearly constant because of active convective mixing (Fig. 2b). The magnitudes of entrainment heat flux in the FF, SF, SB, and SC cases are related to the degree of the mixing of heat in the entrainment zone. More active mixing of heat (higher potential temperature between z_{il} and z_i) in the SB and SC cases than in the other cases is distinct in Fig. 2b. The magnitude of vertical turbulent momentum flux is larger in the SB and SC cases than that in the FF and SF cases (Fig. 2c) because of resolved/modeled pressure drag in the canopy layer. Because of more turbulent surface layer in the SB and SC cases, the mean streamwise velocity is lower than that in the SF case (Fig. 2d). The deceleration in the SB and SC cases induces stronger wind shear in the entrainment zone than in the SF case. Note that the wind shear in the entrainment zone is 0.0122 s^{-1} in the SB case, 0.0141 s^{-1} in the SC case, and 0.0073 s^{-1} in the SF case. Here, the wind shear in the entrainment zone is calculated by dividing the difference in streamwise velocity between the upper and lower limits of entrainment zone by the thickness of entrainment zone (Table 1). The mean streamwise velocity in the SC case is slightly lower in the mixed layer and higher in the canopy

layer than that in the SB case (Fig. 2d). This difference might be attributed to the fact that the vertical variation of drag coefficient is not considered in the SC case.

Vertical velocity fields at $z = 500 \text{ m}$ ($\sim z_i/2$) and the same fields at $z = 1000 \text{ m}$ ($\sim z_i$) in the FF, SF, and SB cases at $t = 6900 \text{ s}$ are plotted in Fig. 3. Convection cells occur in the FF case, and their cellular structure and the circular shape of each cell top are distinct in the x - y planes at $z = 500$ and 1000 m , respectively (Figs. 3a,d). In the SF case, the ratio of friction velocity to convective velocity (0.31) is slightly smaller than 0.35 (Sykes and Henn 1989), the value at which HCRs occur, and intermediate structures between cells and rolls appear. In contrast, HCRs appear in the SB case with their axis slightly inclined toward the north. Note that the ratio of friction velocity to convective velocity in the SB case is 0.34, similar to the value at which HCRs occur (0.35). At $z = 500 \text{ m}$ (in the mixed layer), HCRs are distinct and their spanwise spacing is about twice the inversion height. The spacing of convective rolls observed in this study ($\sim 2z_i$) is similar to the value reported in Kim and Park (2003). At $z = 1000 \text{ m}$ (near the inversion height), alternating updrafts and downdrafts appear mostly above the rising parts of HCRs. This pattern is similar to the wavelike motion occurring with strong wind shear (Sullivan et al. 1998; Kim et al. 2003). This kind of HCRs and wavelike motions at approximately the inversion

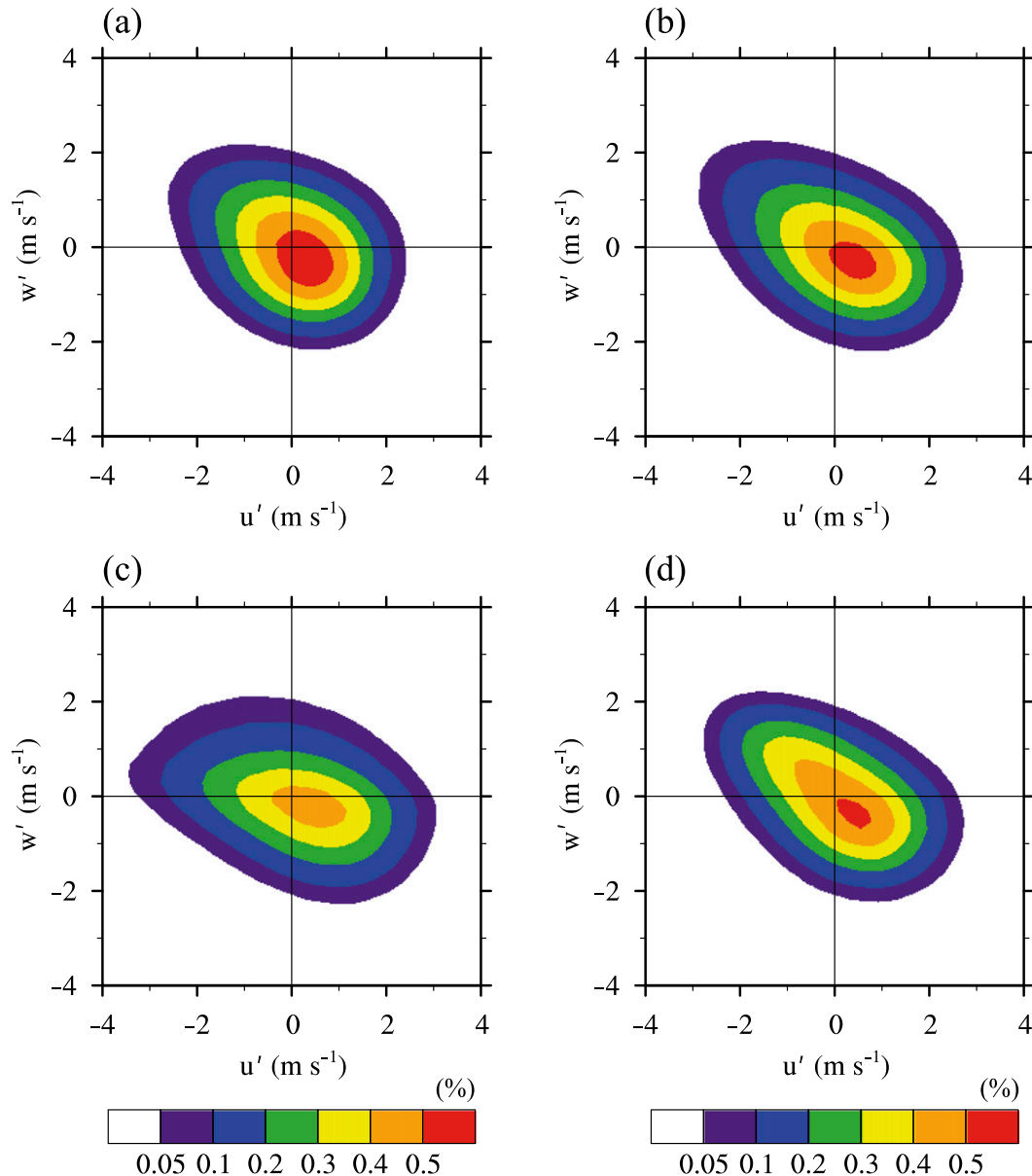


FIG. 7. Fields of the joint probability density of u' and w' at $z = 100$ m in the (a) SF, (b) SSF, (c) SB, and (d) SC cases.

height also appear in the SSF case where the ratio of friction velocity to convective velocity (0.40) is larger than 0.35. In the SC case, however, the intermediate structures between cells and rolls appear in the mixed layer despite the large ratio of friction velocity to convective velocity (0.40).

Figure 4 shows the spectral density fields of vertical velocity at $t = 6900$ s in the SF and SB cases. The spectral density of vertical velocity at each spanwise wavelength λ_y for every streamwise position and height is calculated and the streamwise averages of the spectral

density fields are plotted to demonstrate spanwise-periodic features of HCRs at $t = 6900$ s. The spectral density (or variance) of vertical velocity is high at $(\lambda_y, z) \sim (2000 \text{ m}, 500 \text{ m})$, indicating the dominance of HCRs in the SB case and the dominance of intermediate structures in the SF case. The value of the spectral density around the maximum is larger over a narrower range of spanwise wavelength in the SB case than in the SF case. The spectral density above the inversion height is also higher in the SB case than in the SF case, indicating stronger fluctuations there. It is noticeable that the spectral density

below $z \sim 160$ m is slightly high between $\lambda_y \sim 600$ m and $\lambda_y \sim 800$ m in the SB case. This might be related to turbulent eddies generated around the blocks.

The spanwise-periodic features of HCRs are again demonstrated in the temporally (600 s) averaged fields of space (Δy)-lag cross-correlation coefficient at $z = 500$ m (Fig. 5). The space-lag cross-correlation coefficient of vertical velocity at $(x, y, z) = (x_{\text{ref}}, y, z_{\text{ref}})$ and vertical velocity at $(x, y, z) = (x, y, z_{\text{ref}})$ at each time instant and streamwise position is calculated using the expression $\text{cov}[w(x_{\text{ref}}, y, z_{\text{ref}}), w(x, y + \Delta y, z_{\text{ref}})] / \{\text{var}[w(x_{\text{ref}}, y, z_{\text{ref}})] \text{var}[w(x, y, z_{\text{ref}})]\}^{1/2}$, where x_{ref} and z_{ref} are 7680 and 500 m, respectively. The calculated space-lag cross-correlation coefficients are averaged for 600 s, and they illustrate more distinct HCRs in the SB case than in the other cases. The highly correlated and streamwise-elongated structures do not appear in the SC case despite the inclusion of modeled pressure drag. This indicates that physical blocks play an important role in inducing HCRs. Except the SB case, HCRs are most prominent in the SSF case (Fig. 5b).

Figure 6 shows the vertical profiles of spanwise (at $x = 7680$ m)- and temporally (for 600 s) averaged TKE, skewness of streamwise velocity, and skewness of vertical velocity in the FF, SF, SB, and SSF cases. As the geostrophic wind speed increases from 10 (SF) to 15 m s^{-1} (SSF), TKE increases and TKE in the upper mixed layer and entrainment zone is similar in magnitude to the SB case. The vertical profiles of streamwise velocity skewness indicate that strong negative perturbation events occur in the lower and upper parts of the CBLs in all cases except for in the FF case. Local minimum below $z/z_i = 0.2$ is attributed to ejection eddies induced by the bottom surface (or blocks), and that in the entrainment zone might be related to HCRs or turbulent eddies induced by shear instability in all sheared CBLs. Because of the existence of blocks and the large difference in streamwise velocity in the entrainment zone, infrequent negative perturbations occur more strongly in the SB case than in the other cases. The vertical profiles of vertical velocity skewness in all cases exhibit typical structures of the CBL (i.e., having maximum values at $z/z_i \sim 0.5$). The vertical velocity skewness is nearly constant between $z/z_i = 0.1$ and 0.2 in the SB case. This might be related to ejection eddies induced by blocks as is shown in Fig. 4b.

Figure 7 shows the joint probability density functions (PDFs) of u' and w' at $z = 100$ m (for 600 s) in the SF, SSF, SB, and SC cases. The joint PDF is calculated using the expression $f_{u',w'}(c_i, c_j) = P(c_i - 0.5\Delta c < u' \leq c_i + 0.5\Delta c, c_j - 0.5\Delta c < w' \leq c_j + 0.5\Delta c)$ (Park and Baik 2013). Here, c_i and Δc are i th value of variable c and the spacing of bins (0.2), respectively, and the number of

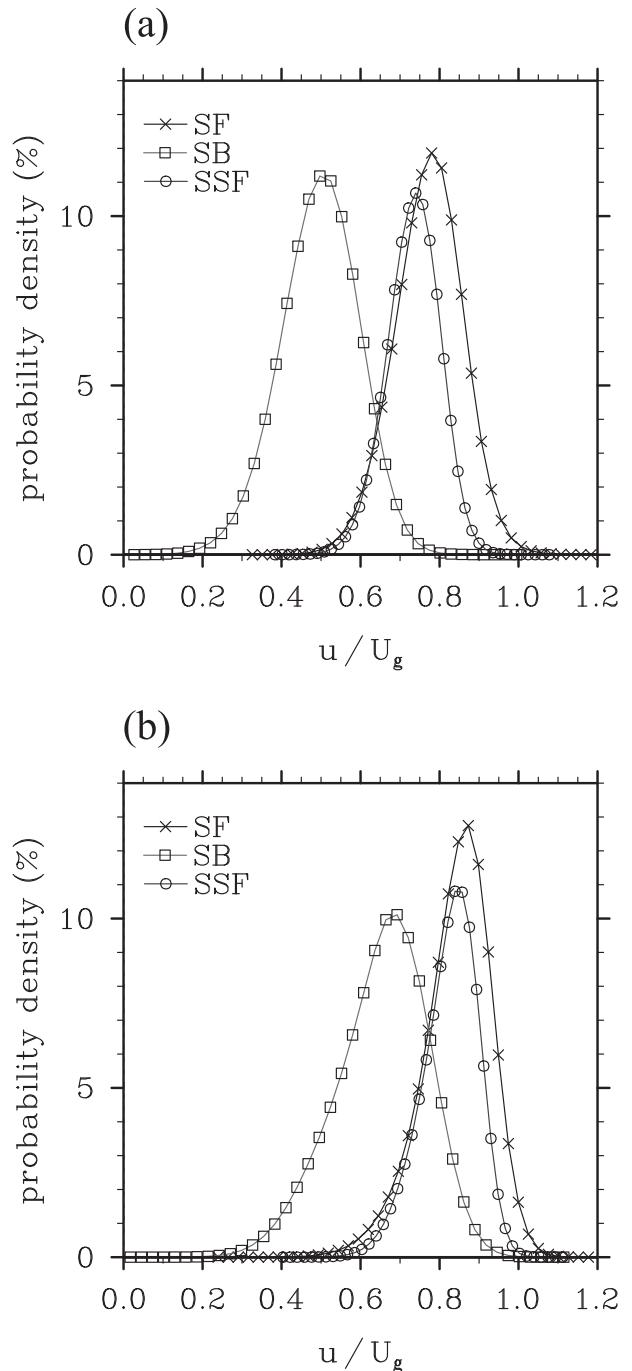


FIG. 8. Probability density distributions of normalized streamwise velocity at (a) $z = 500$ m and (b) $z = 1000$ m in the SF, SB, and SSF cases.

bins in each direction is 50. Following the definition in Raupach (1981), the instantaneous vertical turbulent momentum flux $u'w'$ can be classified into the four turbulent events: outward interaction $u'_+w'_+$, ejection $u'_-w'_+$, inward interaction $u'_+w'_-$, and sweep $u'_-w'_-$. At

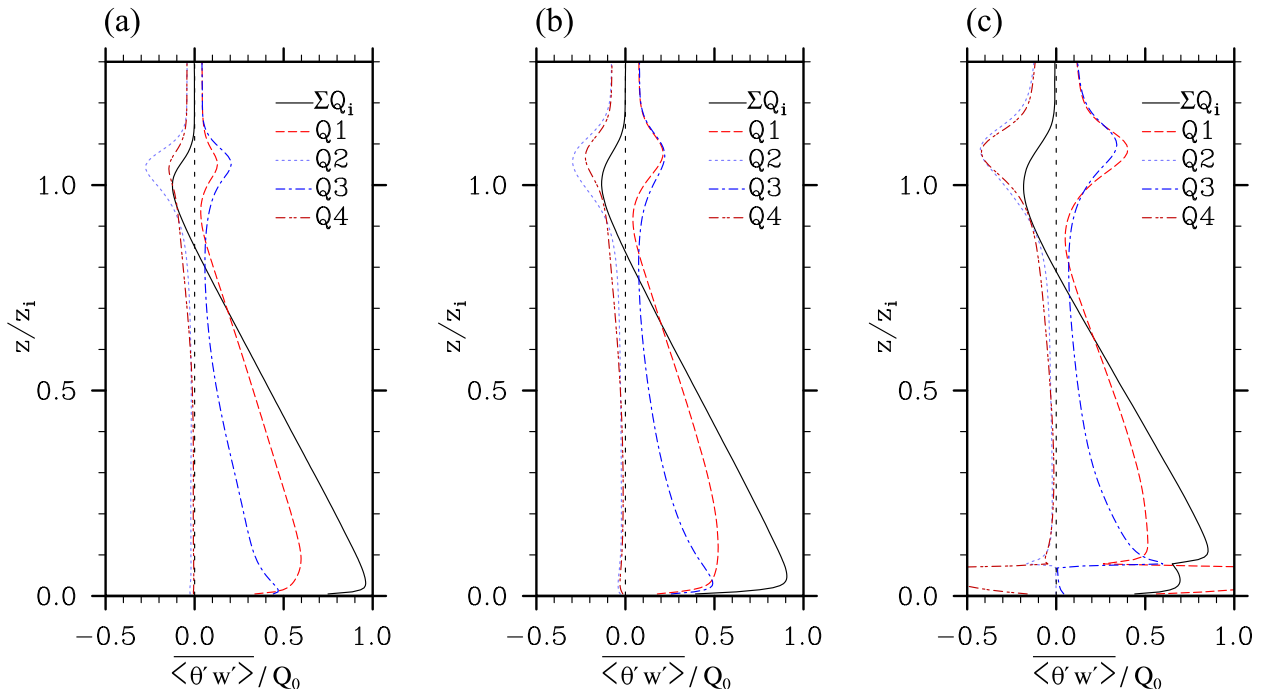


FIG. 9. Vertical profiles of temporally and horizontally averaged vertical turbulent heat flux contributed by the four quadrant events in the (a) FF, (b) SF, and (c) SB cases.

$z = 100$ m, frequent sweeps and less frequent but stronger (farther from the origin) ejections are dominant in transporting momentum downward. In the SB case, the probability (or frequency) of weak sweeps decreases and that of strong ejections increases compared to the other cases. In particular, strong ejections in the SB case tend to occur with large negative u' , corresponding to the large negative u skewness in Fig. 6b. Strong ejections occur more frequently also in the SC case, but the overall distribution of turbulent eddies is not significantly different from that in the SF and SSF cases.

b. Effects of blocks on the entrainment heat flux

Figure 8 shows the PDFs of normalized streamwise velocity u/U_g at $z = 500$ m and the PDFs at $z = 1000$ m in the SF, SB, and SSF cases. Blocks induce turbulent eddies, such as ejections, transporting momentum downward above the blocks and decelerating mean flow in the mixed layer. The PDF at $z = 500$ m in the SB case is quite different from the PDFs in the other cases while the PDF in the SF case is quite similar to the PDF in the SSF case. The decelerated flow in the mixed layer over the block array also decelerates the flow in the entrainment zone. The deceleration in the SB case is distinct at $z = 1000$ m (Fig. 8b).

The vertical profiles of vertical turbulent heat flux contributed by the four quadrant events are plotted in

Fig. 9. The instantaneous vertical turbulent heat flux $\theta'w'$ can be classified into the four quadrant events: warm air rising or ejection ($Q_1: \theta'_+ w'_+$), cool air rising ($Q_2: \theta'_- w'_+$), cool air sinking or sweep ($Q_3: \theta'_- w'_-$), and warm air sinking ($Q_4: \theta'_+ w'_-$) (Sullivan et al. 1998). Below the entrainment zone ($z < z_{il}$), Q_1 and Q_3 contribute to most of the vertical turbulent heat flux in all cases. In the FF case, Q_2 and Q_3 dominate turbulent heat transport in the entrainment zone (Fig. 9a). This kind of transport pattern corresponds to the circular-shaped updrafts surrounded by downdrafts at $z = 1000$ m in Fig. 3d. As the wind shear in the entrainment zone increases, the magnitudes of Q_1 and Q_4 increase and also the magnitude of vertical turbulent heat flux (the sum of fluxes contributed by all the quadrant events) increases in the entrainment zone (Fig. 9). In the SB case, the magnitudes of Q_1 and Q_4 in the entrainment zone increase more than those in the SF case because of the increased wind shear in the entrainment zone. This kind of increasing trend of Q_1 and Q_4 with increasing wind shear is closely related to the mixing of upper warm air by wavelike motions, and this corresponds to the breaking of Kelvin–Helmholtz waves, as reported in Kim et al. (2003).

The different heat transport patterns between the FF and SB cases are again illustrated in Fig. 10. The fields of $\theta'w'$ at $z = 1000$ m and $t = 6900$ s in the FF and SB cases are plotted in Fig. 10. The added contours of vertical

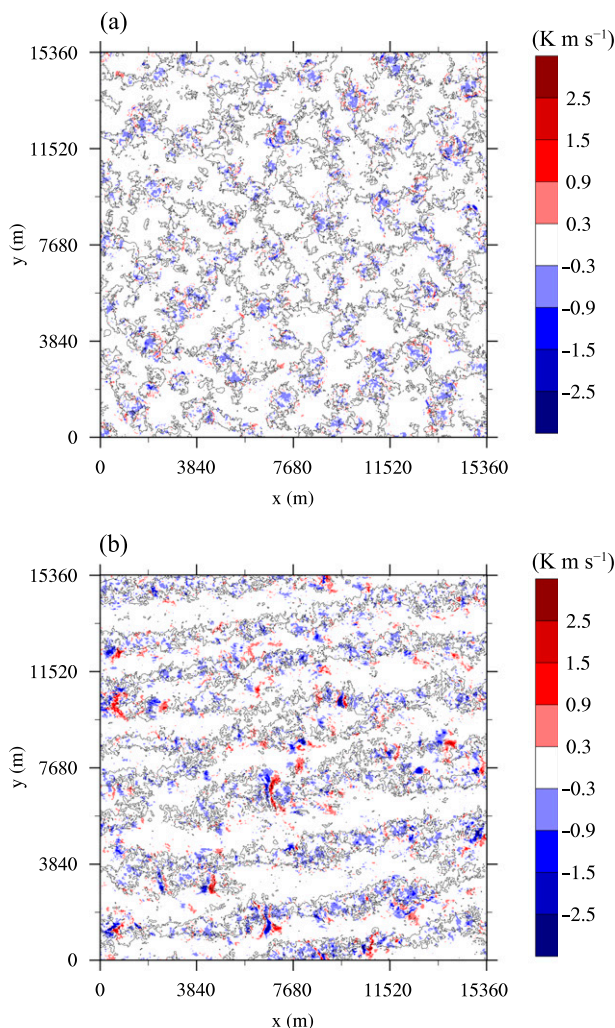


FIG. 10. Fields of $\theta'w'$ at $z = 1000$ m and $t = 6900$ s in the (a) FF and (b) SB cases. The contours of vertical velocity (0.5 m s^{-1}) at $z = 500$ m are added.

velocity (0.5 m s^{-1}) represent the rising parts (at $z = 500$ m) of convection cells in the FF case and those of HCRs in the SB case. In both cases, strong turbulent heat transport events are concentrated on the rising parts of convective flow structures. While the downward turbulent heat transport events (mainly composed of Q_2) dominate over the upward turbulent heat transport events in the FF case, quite strong upward (red) turbulent heat transport events intermittently occur with more frequent downward (blue) turbulent heat transport events in the SB case.

Figure 11 shows the cospectral density fields of vertical velocity and potential temperature at $t = 6900$ s in the SF and SB cases. As in the spectrum fields of vertical velocity shown in Fig. 4, the cospectrum field in the SB case shows more compact shape, centered on

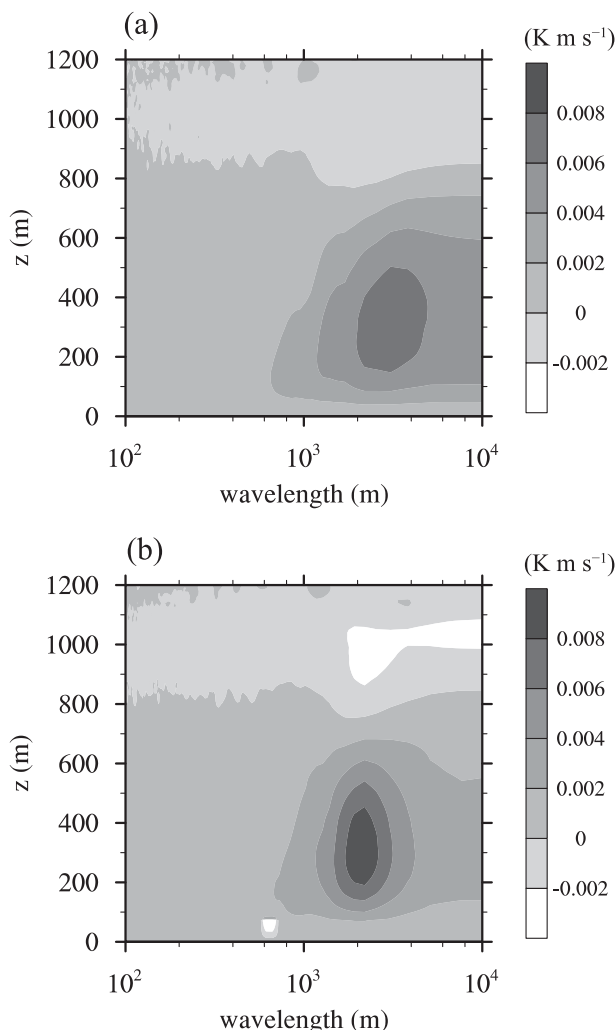


FIG. 11. Cospectral density fields of vertical velocity and potential temperature in the λ_y - z plane at $t = 6900$ s in the (a) SF and (b) SB cases.

$(\lambda_y, z) \sim (2000 \text{ m}, 300 \text{ m})$, than that in the SF case. Particularly in the entrainment zone, the negative cospectral density appears in a larger magnitude in the SB case than in the SF case, indicating stronger downward turbulent heat flux over the HCRs.

Figure 12 shows the ratio of entrainment heat flux to bottom heat flux with the difference in streamwise velocity between the upper and lower limits of the entrainment zone in all cases. As shown in Fig. 8, blocks in the SB case decelerate mixed-layer flow and increase wind shear in the entrainment zone. This kind of the indirect effect of blocks on the entrainment zone corresponds well with the indirect effect of surface shear reported by Conzemius and Fedorovich (2006). In the cases with constant bottom heat flux (0.2 K m s^{-1}), the ratio of entrainment heat flux to bottom heat flux tends

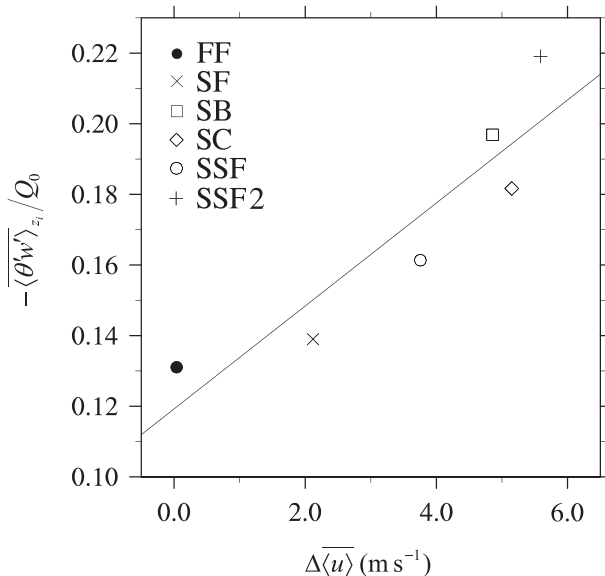


FIG. 12. The ratio of entrainment heat flux to bottom heat flux ($-\langle \theta'w' \rangle_{z_i}/Q_0$) with the difference in streamwise velocity between the upper and lower limits of the entrainment zone in all cases.

to increase linearly with increasing streamwise velocity difference across the entrainment zone (Fig. 12). Also, an approximately linear relation between the ratio of entrainment heat flux to bottom heat flux and wind shear in the entrainment zone is found. To confirm the linear relation, we simulated one more CBL over a flat surface with a geostrophic wind speed of 20 m s^{-1} (SSF2). In the SSF2 case, the ratio of the mixed-layer wind speed to the geostrophic wind speed is similar to the ratios in the SF and SSF cases. However, the absolute value of the streamwise velocity difference across the entrainment zone in the SSF2 case is larger than that in the SB case and the ratio of entrainment heat flux to bottom heat flux in the SSF2 case is also larger than that in the SB case (Fig. 12). Thus, the magnitude of wind shear in the entrainment zone (or velocity jump at the inversion height), as well as the surface shear, is important for parameterizing the entrainment heat flux (Conzemius and Fedorovich 2006). It is also noticeable that the ratio of entrainment heat flux to bottom heat flux in the SB case is slightly larger than that in the SC case, although wind shear in the SB case is smaller than that in the SC case. This can be attributed to the dominant HCRs in the SB case, and these possible impacts of CBL flow structures should be further investigated and included in parameterizing the entrainment heat flux.

4. Summary and conclusions

The effects of urbanlike surface with a block array on the dry convective boundary layer were investigated

using an LES model. A free CBL (FF), a sheared CBL (SF), a strongly sheared CBL (SSF) over flat surfaces, a sheared CBL over a block array (SB), and a sheared CBL over a modeled canopy layer (SC) were simulated. The magnitudes of entrainment heat flux and vertical turbulent momentum flux in the SB case are larger than those in the other cases. Because of the increased surface shear in the SB case, flow in the mixed layer is markedly decelerated and HCRs appear in the mixed layer. In contrast, convection cells occur in the FF case and intermediate structures between cells and rolls occur in the SF case. The intermediate structures (instead of HCRs) also occur over a modeled canopy layer, although the decelerated mixed-layer flow is well simulated in the SC case. Large-scale flow structures in the mixed layer also appear in the spectral density fields of vertical velocity having a spanwise wavelength of approximately $2z_i$. Along with the large-scale secondary circulations, traces of block-induced turbulent eddies are detected in the spectral density fields of vertical velocity and in the vertical profiles of vertical velocity skewness. The decelerated mixed-layer flow in the SB case induces strong wind shear in the entrainment zone and changes turbulence structures there, resulting in stronger entrainment heat flux at the inversion height. The magnitude of the entrainment heat flux in the CBLs linearly increases with increasing wind shear in the entrainment zone in all cases, and the indirect effect of blocks on the entrainment heat flux can be explained again by the linear relationship.

This study demonstrates that in built-up urban areas where the surface roughness is large, CBL flow decelerates and the magnitude of entrainment heat flux increases. In this study, an in-line arranged block array was considered. Flow in the surface layer is quite dependent upon block morphology, and the turbulence structures of the mixed layer (and possibly the entrainment process) might be affected by block morphology too. Further study focusing on the characteristics of block-induced turbulent eddies for various block morphologies is required to understand the interactions of block-induced turbulent eddies and large convective flow structures in the urban planetary boundary layer.

Acknowledgments. The authors are grateful to three anonymous reviewers for providing valuable comments on this work. This work was supported by the National Research Foundation of Korea (NRF) grant funded by the Korea Ministry of Education, Science and Technology (MEST) (Grant 2012-0005674) and also by the Brain Korea 21 Project (through the School of Earth and Environmental Sciences, Seoul National University).

REFERENCES

- Barlow, J. F., G. G. Rooney, S. von Hünenbein, and S. G. Bradley, 2008: Relating urban surface-layer structure to upwind terrain for the Salford experiment (Salfex). *Bound.-Layer Meteor.*, **127**, 173–191, doi:10.1007/s10546-007-9261-y.
- Castillo, M. C., A. Inagaki, and M. Kanda, 2011: The effects of inner- and outer-layer turbulence in a convective boundary layer on the near-neutral inertial sublayer over an urban-like surface. *Bound.-Layer Meteor.*, **140**, 453–469, doi:10.1007/s10546-011-9614-4.
- Coccal, O., A. Dobre, and T. G. Thomas, 2007: Unsteady dynamics and organized structures from DNS over an idealized building canopy. *Int. J. Climatol.*, **27**, 1943–1953, doi:10.1002/joc.1549.
- Conzemius, R. J., and E. Fedorovich, 2006: Dynamics of sheared convective boundary layer entrainment. Part I: Methodological background and large-eddy simulations. *J. Atmos. Sci.*, **63**, 1151–1178, doi:10.1175/JAS3691.1.
- Deardorff, J. W., 1980: Stratocumulus-capped mixed layers derived from a three-dimensional model. *Bound.-Layer Meteor.*, **18**, 495–527, doi:10.1007/BF00119502.
- Emeis, S., K. Baumann-Stanzer, M. Piringer, M. Kallistratova, R. Kouznetsov, and V. Yushkov, 2007: Wind and turbulence in the urban boundary layer—Analysis from acoustic remote sensing data and fit to analytical relations. *Meteor. Z.*, **16**, 393–406, doi:10.1127/0941-2948/2007/0217.
- Harman, I. N., and J. J. Finnigan, 2007: A simple unified theory for flow in the canopy and roughness sublayer. *Bound.-Layer Meteor.*, **123**, 339–363, doi:10.1007/s10546-006-9145-6.
- Inagaki, A., and M. Kanda, 2010: Organized structure of active turbulence over an array of cubes within the logarithmic layer of atmospheric flow. *Bound.-Layer Meteor.*, **135**, 209–228, doi:10.1007/s10546-010-9477-0.
- , M. C. L. Castillo, Y. Yamashita, M. Kanda, and H. Takimoto, 2012: Large-eddy simulation of coherent flow structures within a cubical canopy. *Bound.-Layer Meteor.*, **142**, 207–222, doi:10.1007/s10546-011-9671-8.
- Iwai, H., and Coauthors, 2008: Dual-Doppler lidar observation of horizontal convective rolls and near-surface streaks. *Geophys. Res. Lett.*, **35**, L14808, doi:10.1029/2008GL034571.
- Kanda, M., A. Inagaki, T. Miyamoto, M. Gryschka, and S. Raasch, 2013: A new aerodynamic parametrization for real urban surfaces. *Bound.-Layer Meteor.*, **148**, 357–377, doi:10.1007/s10546-013-9818-x.
- Khanna, S., and J. G. Brasseur, 1998: Three-dimensional buoyancy- and shear-induced local structure of the atmospheric boundary layer. *J. Atmos. Sci.*, **55**, 710–743, doi:10.1175/1520-0469(1998)055<0710:TDBASI>2.0.CO;2.
- Kim, S.-W., and S.-U. Park, 2003: Coherent structures near the surface in a strongly sheared convective boundary layer generated by large-eddy simulation. *Bound.-Layer Meteor.*, **106**, 35–60, doi:10.1023/A:1020811015189.
- , —, and C.-H. Moeng, 2003: Entrainment processes in the convective boundary layer with varying wind shear. *Bound.-Layer Meteor.*, **108**, 221–245, doi:10.1023/A:1024170229293.
- Kropfli, R. A., and N. M. Kohn, 1978: Persistent horizontal rolls in the urban mixed layer as revealed by dual-Doppler radar. *J. Appl. Meteor.*, **17**, 669–676, doi:10.1175/1520-0450(1978)017<0669:PHRITU>2.0.CO;2.
- LeMone, M. A., 1973: The structure and dynamics of horizontal roll vortices in the planetary boundary layer. *J. Atmos. Sci.*, **30**, 1077–1091, doi:10.1175/1520-0469(1973)030<1077:TSADOH>2.0.CO;2.
- Letzel, M. O., M. Krane, and S. Raasch, 2008: High resolution urban large-eddy simulation studies from street canyon to neighbourhood scale. *Atmos. Environ.*, **42**, 8770–8784, doi:10.1016/j.atmosenv.2008.08.001.
- Lin, C.-L., C.-H. Moeng, P. P. Sullivan, and J. C. McWilliams, 1997: The effect of surface roughness on flow structures in a neutrally stratified planetary boundary layer flow. *Phys. Fluids*, **9**, 3235–3249, doi:10.1063/1.869439.
- Macdonald, R. W., 2000: Modelling the mean velocity profile in the urban canopy layer. *Bound.-Layer Meteor.*, **97**, 25–45, doi:10.1023/A:1002785830512.
- Miao, Q., B. Geerts, and M. LeMone, 2006: Vertical velocity and buoyancy characteristics of coherent echo plumes in the convective boundary layer, detected by a profiling airborne radar. *J. Appl. Meteor. Climatol.*, **45**, 838–855, doi:10.1175/JAM2375.1.
- Miao, S., and F. Chen, 2008: Formation of horizontal convective rolls in urban areas. *Atmos. Res.*, **89**, 298–304, doi:10.1016/j.atmosres.2008.02.013.
- Moeng, C.-H., and P. P. Sullivan, 1994: A comparison of shear- and buoyancy-driven planetary boundary layer flows. *J. Atmos. Sci.*, **51**, 999–1022, doi:10.1175/1520-0469(1994)051<0999:ACOSAB>2.0.CO;2.
- Newsom, R., R. Calhoun, D. Ligon, and J. Allwine, 2008: Linearly organized turbulence structures observed over a suburban area by dual-Doppler lidar. *Bound.-Layer Meteor.*, **127**, 111–130, doi:10.1007/s10546-007-9243-0.
- Park, S.-B., and J.-J. Baik, 2013: A large-eddy simulation study of thermal effects on turbulence coherent structures in and above a building array. *J. Appl. Meteor. Climatol.*, **52**, 1348–1365, doi:10.1175/JAMC-D-12-0162.1.
- Piacsek, S. A., and G. P. Williams, 1970: Conservation properties of convection difference schemes. *J. Comput. Phys.*, **6**, 392–405, doi:10.1016/0021-9991(70)90038-0.
- Pino, D., and J. Vilà-Guerau de Arellano, 2008: Effects of shear in the convective boundary layer: Analysis of the turbulent kinetic energy budget. *Acta Geophys.*, **56**, 167–193, doi:10.2478/s11600-007-0037-z.
- Raasch, S., and D. Etling, 1998: Modeling deep ocean convection: Large eddy simulation in comparison with laboratory experiments. *J. Phys. Oceanogr.*, **28**, 1786–1802, doi:10.1175/1520-0485(1998)028<1786:MDOCLE>2.0.CO;2.
- , and M. Schröter, 2001: PALM—A large-eddy simulation model performing on massively parallel computers. *Meteor. Z.*, **10**, 363–372, doi:10.1127/0941-2948/2001/0010-0363.
- Raupach, M. R., 1981: Conditional statistics of Reynolds stress in rough-wall and smooth-wall turbulent boundary layers. *J. Fluid Mech.*, **108**, 363–382, doi:10.1017/S0022212081002164.
- Sullivan, P. P., C.-H. Moeng, B. Stevens, D. H. Lenschow, and S. D. Mayor, 1998: Structure of the entrainment zone capping the convective atmospheric boundary layer. *J. Atmos. Sci.*, **55**, 3042–3064, doi:10.1175/1520-0469(1998)055<3042:SOTEZC>2.0.CO;2.
- Sykes, R. I., and D. S. Henn, 1989: Large-eddy simulation of turbulent sheared convection. *J. Atmos. Sci.*, **46**, 1106–1118, doi:10.1175/1520-0469(1989)046<1106:LESOTS>2.0.CO;2.
- Watanabe, T., 2004: Large-eddy simulation of coherent turbulence structures associated with scalar ramps over plant canopies. *Bound.-Layer Meteor.*, **112**, 307–341, doi:10.1023/B:BOUN.0000027912.84492.54.
- Xie, Z.-T., and I. P. Castro, 2006: LES and RANS for turbulent flow over arrays of wall-mounted obstacles. *Flow, Turbul. Combust.*, **76**, 291–312, doi:10.1007/s10494-006-9018-6.